Am J Transl Res 2026;18(1):797-813
www.ajtr.org /ISSN:1943-8141/AJTR0170427

Original Article

ADSC-derived exosomes inhibit myofibroblast transdifferentiation and attenuate airway stenosis via METTL3-mediated m6A modification of TLR2

Guoying Zhang[1,2], Tingjin Zheng[3], Weifeng Guo[1], Xibin Zhuang[1]

[1]*Department of Pulmonary and Critical Care Medicine, Quanzhou First Hospital Affiliated to Fujian Medical University, Quanzhou 362000, Fujian, China;* [2]*Fujian Key Laboratory of Lung Stem Cells, The Second Affiliated Hospital of Fujian Medical University, Quanzhou 362000, Fujian, China;* [3]*Department of Clinical Laboratory, Quanzhou First Hospital Affiliated to Fujian Medical University, Quanzhou 362000, Fujian, China*

Received December 1, 2025; Accepted January 19, 2026; Epub January 25, 2026; Published January 30, 2026

Abstract: Objective: To investigate the therapeutic potential of adipose-derived stem cell exosomes (ADSC-Exos) in airway repair and the underlying mechanisms, with a particular focus on the role of N6-methyladenosine (m6A) modification. Methods: ADSC-Exos were isolated and characterized via ultracentrifugation. In vitro effects of ADSC-Exos were evaluated using transforming growth factor-β1 (TGF-β1)-induced fibroblast models. A rabbit airway injury model was established, and exosomes were locally administered. Molecular mechanisms were investigated using methylated RNA immunoprecipitation sequencing (MeRIP-seq), RNA-seq, Western blotting, and qRT-PCR. Results: ADSC-Exos significantly upregulated the expression of m6A methyltransferase methyltransferase-like 3 (METTL3) in both in vivo and in vitro experiments. This upregulation further enhanced the m6A methylation level of Toll-like receptor 2 (TLR2) mRNA, leading to decreased TLR2 expression. Additionally, the phosphatidylinositol 3-kinase-protein kinase B (PI3K-AKT) signaling pathway was inhibited, accompanied by decreased expression of the myofibroblast markers α-smooth muscle actin (α-SMA) and Collagen I. Notably, overexpression of METTL3 reversed the inhibitory effects induced by ADSC-Exos on myofibroblast differentiation. Conclusion: ADSC-Exos promote airway repair by upregulating METTL3, which enhances m6A methylation of TLR2 mRNA, downregulates TLR2, and inhibits PI3K-AKT pathway activation, thereby inhibiting myofibroblast differentiation. This study reveals a novel epigenetic mechanism for the treatment of benign airway stenosis (BAS).

Keywords: ADSC-Exos, airway stenosis, TLR2 methylation, PI3K-AKT pathway, transformation of myofibroblasts

Introduction

Benign airway stenosis refers to airway narrowing caused by various mechanical, physical, and chemical factors, including tracheal intubation, tracheotomy, surgery, trauma, inhalation burns, and nonmalignant lesions secondary to chronic airway inflammatory diseases [1-3]. Over the past decade, the fields of respiratory and critical care medicine have advanced rapidly. With notable progress in respiratory therapeutic technologies and the increasing application of complex procedures such as lung transplantation, the incidence of benign airway stenosis has continued to rise [4]. Consequently, airway scar formation and restenosis have emerged as common and pressing clinical challenges. Airway injury repair is initiated by a localized inflammatory response, followed by the proliferation and migration of endothelial cells and fibroblasts, leading to the formation of granulation tissue that fills the tissue defect. As repair progresses, excessive numbers of myofibroblasts are generated, which contract the wound and secrete collagen. Subsequently, granulation tissue undergoes fibrosis, epithelial regeneration occurs, and the extracellular matrix (ECM) is remodeled, ultimately completing the injury repair process [5, 6].

Myofibroblasts are specialized cells that exhibit an intermediate phenotype between fibroblasts and smooth muscle cells. They originate from the proliferation of resident cells, transdif-

https://doi.org/10.62347/XPQC7344

ferentiation of other cell types (e.g., fibroblasts), and recruitment of circulating precursor cells. Myofibroblasts are characterized by robust ECM secretion, expression of α-smooth muscle actin (α-SMA), and strong contractile capacity. Consequently, they play a crucial role in pathophysiological processes, such as wound healing, scar formation, and pulmonary fibrosis [7]. Excessive transdifferentiation of myofibroblasts, driven by activation of signaling pathways including transforming growth factor-β (TGF-β), angiotensin II, and endothelin-1, results in abnormal collagen deposition, disordered ECM architecture, and sustained matrix contraction. These changes constitute the pathological basis of airway scar formation and restenosis [8, 9]. Therefore, effectively inhibiting fibroblast-to-myofibroblast transdifferentiation and promoting myofibroblast apoptosis represent promising strategies for improving airway repair and optimizing clinical outcomes.

Adipose-derived stem cells (ADSCs) are adult multipotent stem cells that play an important role in regulating tissue repair [10]. In addition to their capacity to differentiate into multiple cell types and replace damaged tissue, their paracrine activity represents another predominant mechanism underlying their therapeutic effects [11-13]. A key component of this paracrine activity is the secretion of exosomes-vesicular structures with a diameter of 30-100 nm that are released through intracellular pathways. These exosomes are enclosed by a phospholipid bilayer and contain various bioactive substances, including lipids, proteins, and nucleic acids. Mesenchymal stem cell (MSC)-derived exosomes promote wound healing, inhibit scar formation, and optimize tissue repair by delivering functional molecules to target cells [14-16].

N6-methyladenosine (m6A) is the most prevalent modification of eukaryotic mRNA and involves methylation of the nitrogen at the sixth position of adenine residues [17]. METTL3-mediated m6A modification serves as a critical regulator of diverse biological processes and developmental pathways in eukaryotes, including circadian rhythm regulation, DNA damage responses, stem cell self-renewal and pluripotency, maternal-zygotic transition, neural function regulation, sex determination in *Drosophila*, and early embryonic development in mice. Accumulating evidence indicates that METTL3 is also critically involved in fibrotic diseases. Specifically, deletion of METTL3 in renal fibroblasts reduces m6A methylation and exacerbates TGF-β1-induced collagen deposition [18]. Moreover, in respiratory diseases, MSC-derived exosomes alleviate asthma-associated airway remodeling by delivering METTL3-enriched vesicles that enhance m6A modification of proinflammatory genes [19].

This study aimed to investigate whether METTL3-mediated m6A modification is involved in the inhibitory effects of ADSC-derived exosomes (ADSC-Exos) on fibroblasts-to-myofibroblast transdifferentiation and whether this mechanism contributes to attenuation of airway scar formation. To elucidate the underlying molecular mechanisms, high-throughput methylated RNA immunoprecipitation sequencing (MeRIP-seq), RNA sequencing (RNA-Seq), bioinformatics analyses, and functional phenotype assays were performed using *in vitro* cell models. Additionally, this study seeks to provide a theoretical foundation for the application of ADSC-Exos in the prevention and treatment of airway scar formation. Elucidating the regulatory mechanisms and downstream targets of METTL3 may further support the development of standardized stem cell-derived component therapies for common fibrotic diseases.

Materials and methods

ADSC culture

ADSCs were harvested from the inguinal subcutaneous adipose tissue of New Zealand white rabbits [20]. Primary ADSCs were isolated by enzymatic digestion using 0.1% type I collagenase, and digestion was terminated by the addition of serum (SKU: SH30084.03, Hyclone, USA). After 16 days of culture, cells were passaged using trypsin (SKU: 25200072, GIBCO, USA). Third-passage ADSCs were then washed with PBS (SKU: E607008, Sangon Biotech, Shanghai). The ADSC phenotype was confirmed by flow cytometry using antibodies against CD90, CD73, CD105, CD44, and CD45, as previously described [21].

Lipogenic, osteogenic, and chondrogenic differentiation of ADSCs

ADSCs were seeded into 6-well plates and cultured at 37°C with 5% CO_2 for 24 h. The culture medium was then replaced with adipogenic induction medium (AIM), osteogenic induction medium (OIM), or chondrogenic induction medium (CIM). The induction media were refreshed every three days, while control cells were maintained in standard culture medium. Adipogenic differentiation was assessed two weeks after induction using Oil Red O staining. Osteogenic differentiation was verified after three weeks using Alizarin Red staining. Chondrogenic differentiation was verified after four weeks using Alcian Blue staining.

Exosome isolation and characterization

Exosomes were harvested from thawed ADSC-conditioned culture supernatant using differential centrifugation. The supernatant was sequentially centrifuged at 2,000×g for 30 minutes and then at 10,000×g for 45 minutes at 4°C to remove cells and cellular debris, followed by filtration through a 0.45 μm membrane. The filtrate was subsequently subjected to ultracentrifugation at 100,000×g for 70 min at 4°C using fixed-angle (FA) rotors. The resultingpellet was washed once with PBS and centrifuged again under the same conditions. The final exosome pellet was resuspended in 150 μL of pre-cooled PBS for subsequent use. Exosome morphology was examined by transmission electron microscopy (TEM; Hitachi, 100 kV) following negative staining with uranyl acetate. Nanoparticle tracking analysis (NTA) was performed to evaluate particle size distribution and concentration (Granulometry Instrumentation Co., Ltd.).

Animal experiments

Young adult New Zealand White rabbits (approximately 8 months old, weighing 4.0-5.0 kg) were purchased from SLAC Laboratory Animal Co., Ltd. (Shanghai, China; License No. SCXK (Shanghai) 2022-0004). All experimental procedures were approved by the Experimental Animal Ethics Committee of Quanzhou Medical College (Approval No. 2024044).

Animals were anesthetized with sodium pentobarbital (50 mg/kg) prior to the procedure. Under endoscopic guidance, local multipoint injections of ADSC-derived exosomes were administered around the narrowed tracheal segment at four sites (anterior, posterior, medial, and lateral) (Figure S1). The exosome dosage was determined based on published literature [20, 22, 23]. Approximately 50 μg of exosomes, equivalent to 1.2×10^7 particles, were injected at each site. Each rabbit received a total of 200 μg of exosomes dissolved in 200 μL of PBS (corresponding to approximately 4.8×10^7 particles), as determined by the BCA assay (Figure S3; Table S2) [24].

For ADSC isolation from healthy rabbits and for terminal analysis of the *in vivo* airway injury model (performed on day 14 after exosome treatment), euthanasia was conducted by intravenous injection of sodium pentobarbital (100 mg/kg) via the marginal ear vein. Death was confirmed by irreversible cessation of spontaneous respiration and cardiac activity, loss of corneal and pupillary reflexes, and development of cyanosis, monitored continuously for 5-10 min.

Flow cytometry

Adherent cells were collected by trypsin digestion, centrifuged at 800×g for 6 min, washed, and resuspended in sterile PBS. Cells were stained with fluorescein isothiocyanate-conjugated (FITC)-conjugated monoclonal antibodies against CD90, CD73, CD105, CD44, and CD45 for 45 min at 4°C. Isotype-matched antibodies were used as negative controls. Finally, cells were analyzed by flow cytometry [25].

Immunofluorescence

Adherent cells (1×10^4 cells/mL) were seeded into 24-well plates. After 24 h of induction, cells were fixed with pre-cold methanol for 10 min and blocked with 5% fetal bovine serum (FBS). Cells were then incubated overnight with an α-SMA-PE antibody and observed under a fluorescence microscope [26].

Western blotting

After total cellular protein extraction, proteins were separated by electrophoresis and transferred to a polyvinylidene fluoride (PVDF) membrane (SKU: FPV403030, JITE Biofiltration Co., Ltd., Guangzhou). The membrane was blocked

at room temperature for 1 h and then incubated overnight at 4°C with primary antibodies against HSP70, CD63, TSG101, METTL3, α-SMA, β-actin, and GAPDH. Afterward, membranes were incubated with peroxidase-labeled secondary antibodies at room temperature for 2 h. Protein signals were developed using enhanced chemiluminescence (ECL) reagents and visualized with a Bio-Rad Gel Doc EQ system. Quantification of gray-scale values was performed using ImageJ software.

CCK-8

Cells were seeded at a density of 8,000 cells per well in 96-well plates, with three replicate wells per group. STM2457 (SKU: A1472918, Ambeed Inc, USA), a highly selective and potent METTL3 inhibitor, has been extensively validated in multiple disease models, including cancers [27], viral infections [28], and metabolic disorders [29]. STM2457 was diluted to final concentrations of 0.156, 0.3125, 0.625, 1.25, 2.5, 5, 10, 50, and 100 μM and vortexed thoroughly. The final concentration of TGF-β in the cell culture medium was 10 ng/mL, and cells were cultured for an additional 48 h [30].

Subsequently, cell proliferation was assessed using the Cell Counting Kit-8 (CCK-8) assay (SKU: CK04, Tong Ren Chemical, Japan). Absorbance was measured at 450 nm using a microplate reader (Beijing Kaiao Science and Technology Development Co. Ltd.).

Cell transfection

According to the manufacturer's instructions, 200 μL of jetPRIME buffer was added to an Eppendorf tube, followed by the recommended amount of plasmid DNA: OE-NC (overexpression-negative control; pcDNA3.1(+) empty vector), OE-METTL3, or OE-TLR2 (2 μg each), or NC siRNA (negative control siRNA) or METTL3 siRNA (100 ng) [31]. The siRNA sequences are listed in Table S1. The mixture was gently vortexed and combined with 4 μL of jetPRIME reagent. The transfection mixture was then added dropwise to the existing cell culture medium. After 5 h of incubation at 37°C in 5% CO_2, subsequent assays were performed.

Wound healing assay

A Wound healing assay was performed to establish an *in vitro* co-culture model of ADSC-Exos and fibroblasts (SKU: AW-PT092, AnWei Bio-technology Co., Shanghai) to assess the effects of ADSC-Exos on fibroblast-to-myofibroblast trans differentiation. Rabbit skin fibroblasts were seeded into 6-well plates at a density of 4×10^5 cells/well. Upon reaching 85-90% confluence, cells were transfected and divided into five groups: Blank, TGF-β (10 ng/mL), TGF-β+ADSC-Exos+NC OE, TGF-β+ADSC-Exos+TLR2 OE, and TGF-β+ADSC-Exos+STM-2457 (10 μM). A linear scratch was created in the cell monolayer using a sterile 10 μL pipette tip 4-6 h after transfection, ensuring a uniform scratch width across groups. The culture medium was then replaced with fresh medium according to the assigned groups. Cells were incubated at 37°C in a humidified atmosphere containing containing 5% CO_2, and wound closure was assessed at 0, 24, and 48 h [32].

Real-time quantitative PCR (RT-qPCR)

Total RNA was extracted using an RNAprep FastPure Tissue & Cell Kit (SKU: TSP413, Prime Biotechnology Co., Ltd., Beijing). Briefly, genomic DNA was removed in single step using SynScript® III RT SuperMix for qPCR (+gDNA Remover) (SKU: TSK314M, Prime Biotechnology Co., Ltd., Beijing). RT-qPCR was performed using ArtiCanA™ SYBR qPCR Mix (SKU: TSE501, Prime Biotechnology Co., Ltd., Beijing) on an ABI-ViiA 7 Real-Time PCR System (ABI, USA). *GAPDH* was used as the internal reference gene. Relative gene expression levels were quantified using the $2^{-\Delta\Delta Ct}$ method. All primers (**Table 1**) were synthesized by Tsingke (Beijing, China).

qPCR for m6A

m6A levels were measured using the EpiSELECT™ m6A Site Identification Kit (SKU: R202106M-01, Epigenetics Biotechnology Co., China) according to the manufacturer's instructions. Relative m6A methylation levels were determined based on cycle threshold (Ct) differences reflecting methylation-dependent amplification efficiency (https://www.epibiotek.com/biaoguanzhuanluzu/detail/225).

MeRIP-seq

Total cellular RNA was extracted using TRIzol reagent (SKU: 15596018, Invitrogen, USA). RNA concentration was quantified using a Qubit RNA HS Assay Kit (SKU: Q32852,

Table 1. Primers used for RT-qPCR

Primer	*Forward sequence (5'-3')*	*Reverse sequence (5'-3')*
METTL3	ACCTATGCTGACCATTACCAAG	CTGTTGGTTCAGAAGGCTCTC
ACTA2	CCGACCGAATGCAGAAGGA	ACGCTGAGTAAGAGGAGGAAAG
COL1A1	GCTGGCTGGCTGGCTGG	CAGGTCCACAGGTCCACAGGTCCAC
TLR2	CCTGGACAAGGAGGTGAACA	TGCATTGTCACTGGTGAAGG
PIK3CA	GAGGAGCTGGTGGATGTTGT	CAGGTGAGGTTGTTGTAGGC
AKT	GGACAACCGCCATCCAGACT	GCCAGGGACACCTCCATCTC
GAPDH	CGGAGTCAACGGATTTGGTCGTAT	AGCCTTCTCCATGGTGGTGAAGAC

Invitrogen, USA). Total RNA (10 ug) was fragmented using 10× fragmentation buffer, and the reaction was terminated with 0.5 M EDTA. Methylated RNA fragments were immunoprecipitated using the Epi™ m6A Immunoprecipitation Kit (SKU: R1804, Epigenetics Biotechnology Co., China). Both input (non-immunoprecipitated) samples and m6A-immunoprecipitated samples underwent 150-bp paired-end sequencing on an Illumina NovaSeq 6000 platform (Illumina, USA).

RNA-seq

The RNA input used for MeRIP-seq was subjected to mRNA-seq analysis. mRNA was isolated using Epi™ mRNA Capture Beads (SKU: R2020-96, Epigenetics Biotechnology Co., China). The captured mRNA was then used for library construction with the Epi™ mRNA Library Fast kit (SKU: R1810, Epigenetics Biotechnology Co., China) according to the manufacturer's instructions. Briefly, mRNA was fragmented by adding 3× Frag/Prime Buffer, followed by incubation at 94°C for 6 min and immediate cooling on ice. First-strand cDNA synthesis was performed by adding actinomycin D (5 mg/mL), 1st Strand Buffer 2, reverse transcriptase, and RNase inhibitor, followed by sequential incubation at 25°C for 10 min, 42°C for 15 min, and 70°C for 15 min, and subsequent cooling on ice. Second-strand cDNA synthesis was carried out by adding 2nd Strand Buffer 2 (with dUTP) and 2nd Strand Enzyme Mix, followed by incubation at 16°C for 30 min and 72°C for 15 min. Adapter ligation was performed by adding Ligation Buffer 3, EPI DNA Ligase, and adapter, followed by incubation at 22°C for 15 min. The ligated products were purified using Epi™ DNA Clean Beads (SKU: R1809, Epigenetics Biotechnology Co., China). PCR amplification was conducted using 2×HiFi PCR Mix, heat-labile uracil-DNA glycosylase (UDG), and index primers. The amplified libraries were purified again using Epi™ DNA Clean Beads. Library quality and fragment size distribution were assessed using a Bioptic Qsep100 Analyzer to confirm that the libraries were within the expected size range. Finally, sequencing was performed on a NovaSeq high-throughput sequencer in PE150 mode.

Statistical analysis

Data analysis was performed using SPSS 25.0 and GraphPad Prism 10.0. Data are presented as the mean ± standard error of the mean (SEM). The Shapiro-Wilk test was used to assess data normality. Comparisons between two groups were conducted using an unpaired two-tailed *t*-test. For single-factor multiple-group comparisons, one-way analysis of variance (ANOVA) was performed, followed by Tukey's or Dunnett's post-hoc tests, as appropriate. For experiments involving two independent variables, two-way ANOVA was applied with Sidak's or Tukey's post-hoc test. For longitudinal observations from the same subjects, repeated measures ANOVA was used. A P value <0.05 was considered statistically significant.

Results

Isolation and characterization of ADSCs and ADSC-Exos

ADSCs were isolated from rabbit subcutaneous adipose tissue and characterized by flow cytometry. The cells were positive for CD44, CD73, CD90, and CD105, but negative for CD45 (**Figure 1A**). Morphologically, ADSCs exhibited a typical fibroblast-like, spindle-shaped appearance (**Figure 1B**). Their multipotent differentiation capacity was confirmed by Oil Red O staining for adipogenic differentiation, Alizarin Red staining for osteogenic differentiation, and Alcian Blue staining for chondrogenic differentiation (**Figure 1C-E**). Transmission electron microscopy revealed that ADSC-derived exosomes exhibited a characteristic cup-shaped morphology (**Figure 1F**). Nanoparticle tracking analysis indicated that

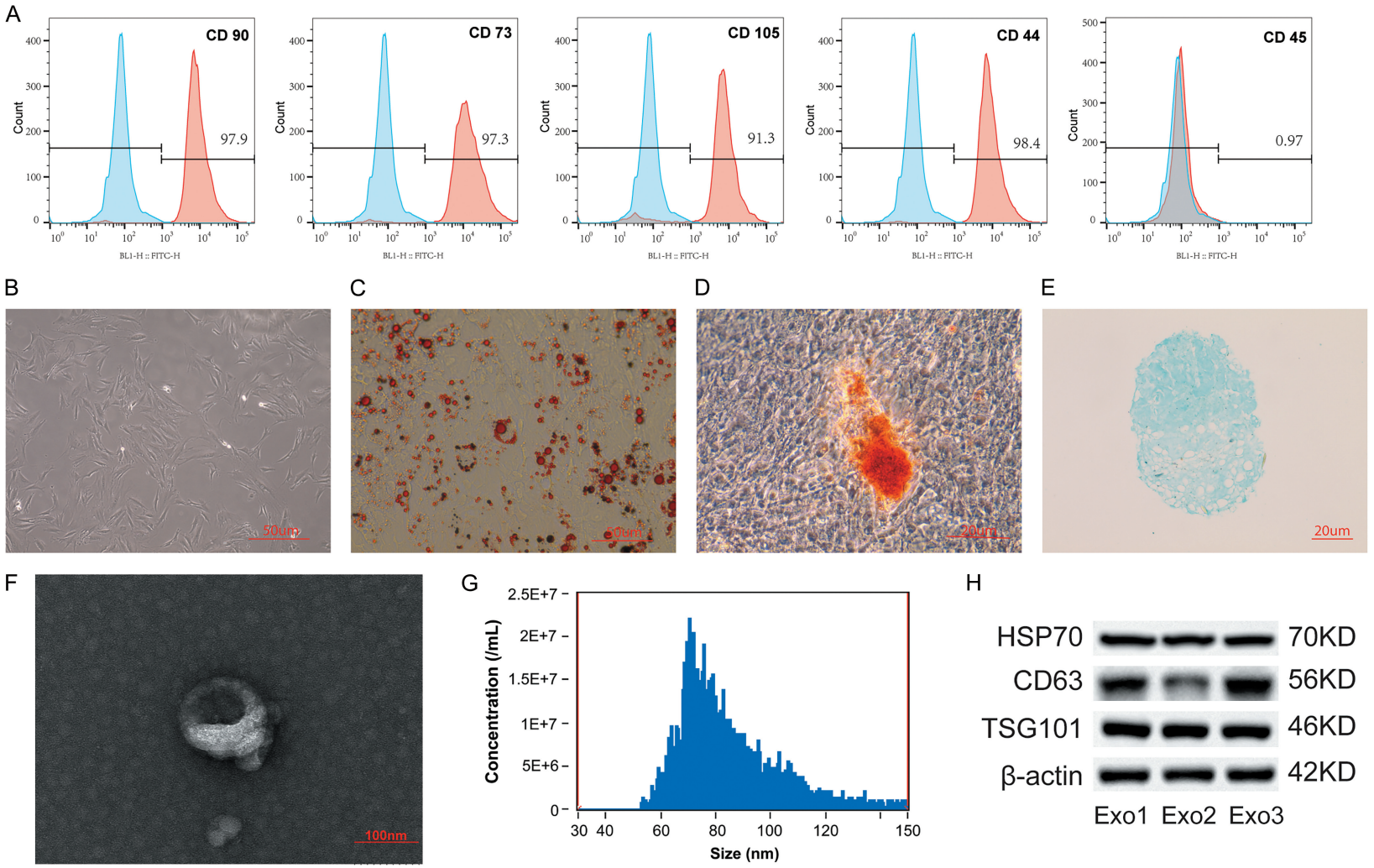

Figure 1. Isolation and characterization of ADSCs and ADSC-derived exosomes. (A) Flow cytometric identification of ADSC surface markers: CD90(+), CD73(+), CD105(+), CD44(+), CD45(-); (B) ADSC culture and purification; (C) Adipogenic differentiation confirmed by Oil red O staining; (D) Osteogenic differentiation confirmed by Alizarin Red staining; (E) Chondrogenic differentiation confirmed by Alcian Blue staining; (F) Transmission electron microscopy showing the morphology of ADSC-derived exosomes (ADSC-Exos); (G) Nanoparticle tracking analysis of ADSC-Exos; (H) Western blot analysis of exosomal marker proteins HSP70, CD63, and TSG101. Notes: ADSC, adipose-derived stem cells; Exos, exosomes. Data are presented as mean ± SEM (n=3). Comparisons between two groups were performed using unpaired two-tailed *t*-tests.

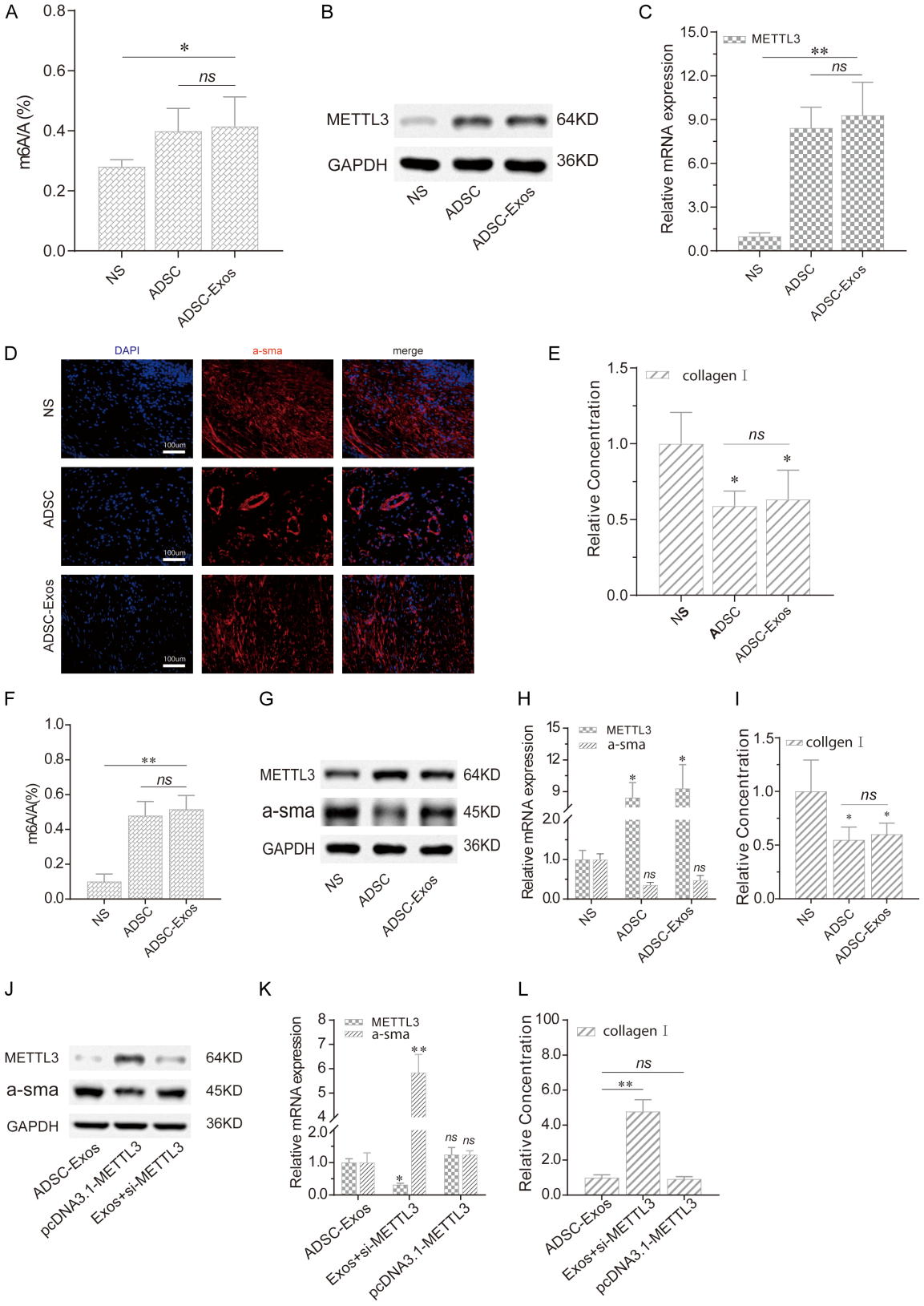

Figure 2. ADSCs and ADSC-Exos inhibit myofibroblast transdifferentiation via METTL3 regulation. (A) m6A methylation levels in airway repair tissues after intervention (n=6); (B) METTL3 protein expression in airway tissues detected by Western blotting (n=3); (C) METTL3 mRNA expression in airway tissues detected by qRT-PCR (n=6); (D) Immuno-

fluorescence staining of the myofibroblast marker α-SMA (n=3); (E) Relative quantification of collagen I, a functional indicator of myofibroblasts, in airway tissues measured by ELISA, (n=6); (F) m6A methylation levels in myofibroblasts after ADSC-Exos treatment (n=6); (G) METTL3 and α-SMA protein expression in myofibroblasts after ADSC-Exos treatment detected by Western blotting (n=3); (H) METTL3 and α-SMA mRNA expression in myofibroblasts after ADSC-Exos treatment detected using qRT-PCR (n=6); (I) Collagen I expression in myofibroblasts after ADSC-Exos intervention measured by ELISA (n=6); (J, K) Protein (J) and mRNA (K) expression levels of METTL3 and α-SMA in myofibroblasts following METTL3 knockdown or overexpression under ADSC-Exos treatment (n=6); (L) Collagen I expression in myofibroblasts following METTL3 knockdown or overexpression measured by ELISA (n=6). Notes: ADSC, adipose-derived stem cells; Exos, exosomes. Data are presented as mean ± SEM. For multiple-group comparisons, one-way ANOVA with Tukey's post hoc test was used. *P<0.05, **P<0.01, ns: not significant.

their particle size distribution primarily ranged from 40 to 120 nm (**Figure 1G**). Western blotting further confirmed the expression of exosomal markers, including HSP70, CD63, and TSG101 (**Figure 1H**).

An in vivo airway injury model was established in rabbits via transoral nylon brush abrasion [33]. Model animals (n=18) were randomly divided into three groups and received local endoscopy-guided injections of normal saline (NS), ADSCs, or ADSC-Exos for one week. The results showed that both ADSC and ADSC-Exos treatments significantly increased total m6A levels and METTL3 expression in repaired airway tissues (**Figure 2A-C**). Concurrently, the expression of myofibroblast markers α-SMA and type I collagen was markedly reduced (**Figure 2D**, **2E**).

To further elucidate the underlying mechanism, fibroblasts were isolated from airway repair tissues and subsequently co-cultured with ADSCs or treated with ADSC-Exos. Elevated m6A levels were observed in both the ADSC and ADSC-Exos groups (**Figure 2F**), along with increased METTL3 expression and decreased α-SMA and type I collagen expression (**Figure 2G-I**). Gain- and loss-of-function experiments targeting METTL3 further confirmed its critical role in this process. Specifically, METTL3 knockdown by siRNA in ADSC-Exos-treated fibroblasts increased α-SMA and collagen I expression (**Figures 2J-L**, S2), whereas METTL3 overexpression produced the opposite effect, demonstrating that ADSC-Exos inhibit fibroblast-to-myofibroblast transformation in a METTL3-dependent manner.

MeRIP-seq analysis

To identify key regulators involved in the inhibitory effects of ADSC-Exos on myofibroblast transformation, total RNA was extracted from myofibroblasts before and after ADSC-Exos treatment and subjected to MeRIP-seq analysis. Comparative analysis revealed a predominance of hypermethylated over demethylated genes in myofibroblasts following ADSC-Exos treatment (**Figure 3A**). The largest number of differential m6A peak distributions was observed on chromosome 13 (**Figure 3B**). Most differential peaks spanned one to four exons (**Figure 3C**). Motif analysis identified the top two enriched m6A motifs in myofibroblasts before and after ADSC-Exos treatment (**Figure 3D**, **3E**). Functional enrichment analysis revealed RNA processing and intracellular transport as the most significantly enriched biological processes associated with differential m6A peaks (**Figure 3F**). In addition, KEGG pathway analysis showed significant enrichment in pathways related to regulation of the actin cytoskeleton, myocyte cytoskeleton, and other signaling pathways (**Figure 3G**). Collectively, these findings suggest that ADSC-Exos may regulate fibroblast-to-myofibroblast transition through epigenetic modulation of m6A methylation.

RNA-seq analysis

To identify genes regulated by ADSC-Exos, RNA-seq analysis was performed using the corresponding input samples from the MeRIP-seq experiments. Principal component analysis demonstrated clear clustering of myofibroblast samples before and after ADSC-Exos treatment (**Figure 4A**). Consistently, hierarchical clustering heatmap analysis showed a more concentrated distribution of gene expression profiles within each group (**Figure 4B**). Differential expression analysis revealed comparable numbers significantly upregulated and downregulated genes in myofibroblasts following ADSC-Exos treatment (**Figure 4C**). Gene Ontology (GO) enrichment analysis of differentially expressed genes indicated significant enrichment in biological processes such as

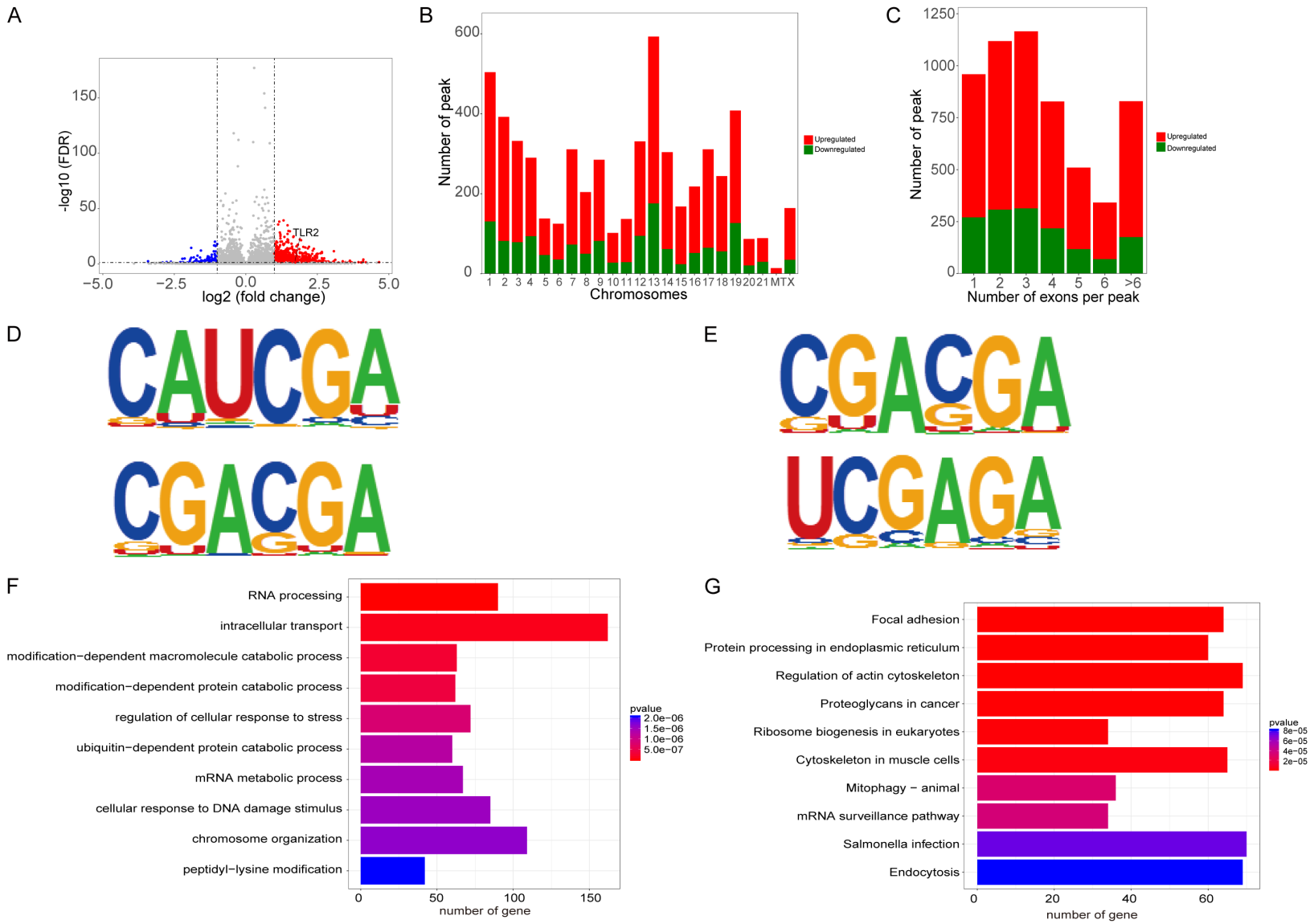

Figure 3. MeRIP-seq analysis (n=3). (A) Volcano plot showing differentially methylated m6A peaks; (B) Distribution m6A peak numbers across chromosomes; (C) Distribution of exon numbers per m6A peak; (D, E) Top two enriched m6A motifs in the control (D) and ADSC-Exos treatment (E) groups; (F) Gene Ontology (GO) enrichment analysis of differentially methylated m6A-associated genes; (G) yoto Encyclopedia of Genes and Genomes (KEGG) pathway enrichment analysis of differentially methylated m6A-associated genes. Notes: GO, Gene Ontology; KEGG, Kyoto Encyclopedia of Genes and Genomes.

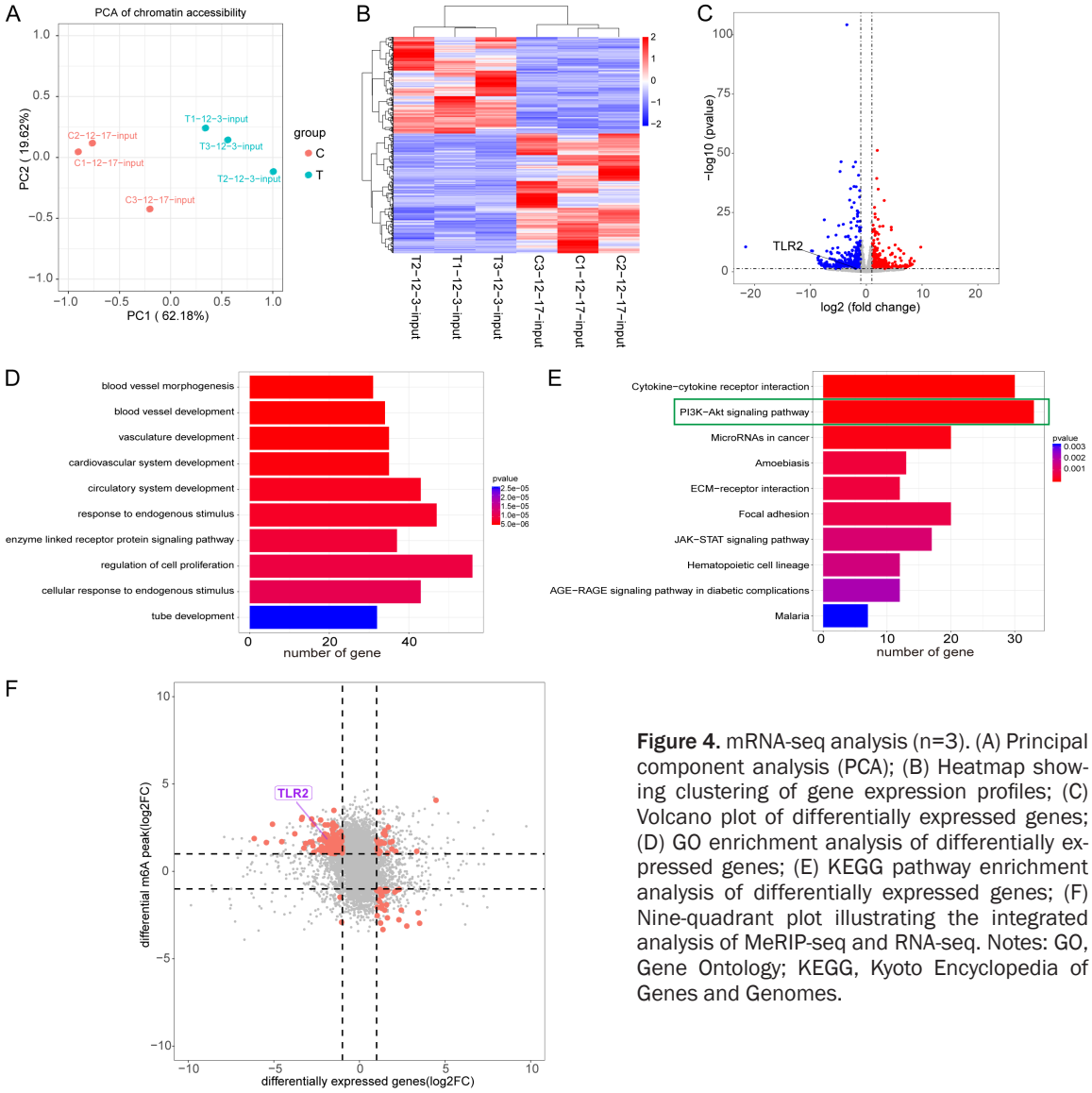

Figure 4. mRNA-seq analysis (n=3). (A) Principal component analysis (PCA); (B) Heatmap showing clustering of gene expression profiles; (C) Volcano plot of differentially expressed genes; (D) GO enrichment analysis of differentially expressed genes; (E) KEGG pathway enrichment analysis of differentially expressed genes; (F) Nine-quadrant plot illustrating the integrated analysis of MeRIP-seq and RNA-seq. Notes: GO, Gene Ontology; KEGG, Kyoto Encyclopedia of Genes and Genomes.

circulatory system development and response to endogenous stimuli (**Figure 4D**). Notably, KEGG pathway analysis highlighted the PI3K-AKT signaling pathway as one of the most significantly affected pathways following ADSC-Exos treatment (**Figure 4E**), suggesting a role for ADSC-Exos in modulating fibroblast injury-related signaling networks.

Integrated analysis of MeRIP-seq and RNA-seq data revealed that the largest subset of genes exhibited both increased m6A methylation and significantly reduced mRNA expression in myofibroblasts after ADSC-Exos treatment (**Figure 4F**). Among these genes, the m6A methylation level of Toll-like receptor 2 (TLR2) was significantly increased, whereas TLR2 mRNA expression was markedly reduced. Given that TLR2 was enriched in the PI3K-AKT signaling pathway, it was selected as a candidate target gene for further mechanistic investigation.

ADSC-Exos suppress myofibroblast transformation via TLR2-dependent modulation of the PI3K-AKT pathway

To investigate whether ADSC-Exos inhibit myofibroblast transformation through modulation of TLR2 methylation and the PI3K-AKT pathway, a TLR2 overexpression vector was constructed (**Figure 5A**) and transfected into primary fibroblasts. Successful overexpression was confirmed at both mRNA and protein levels (**Figure 5B**, **5C**). In parallel, the METTL3 inhibi-

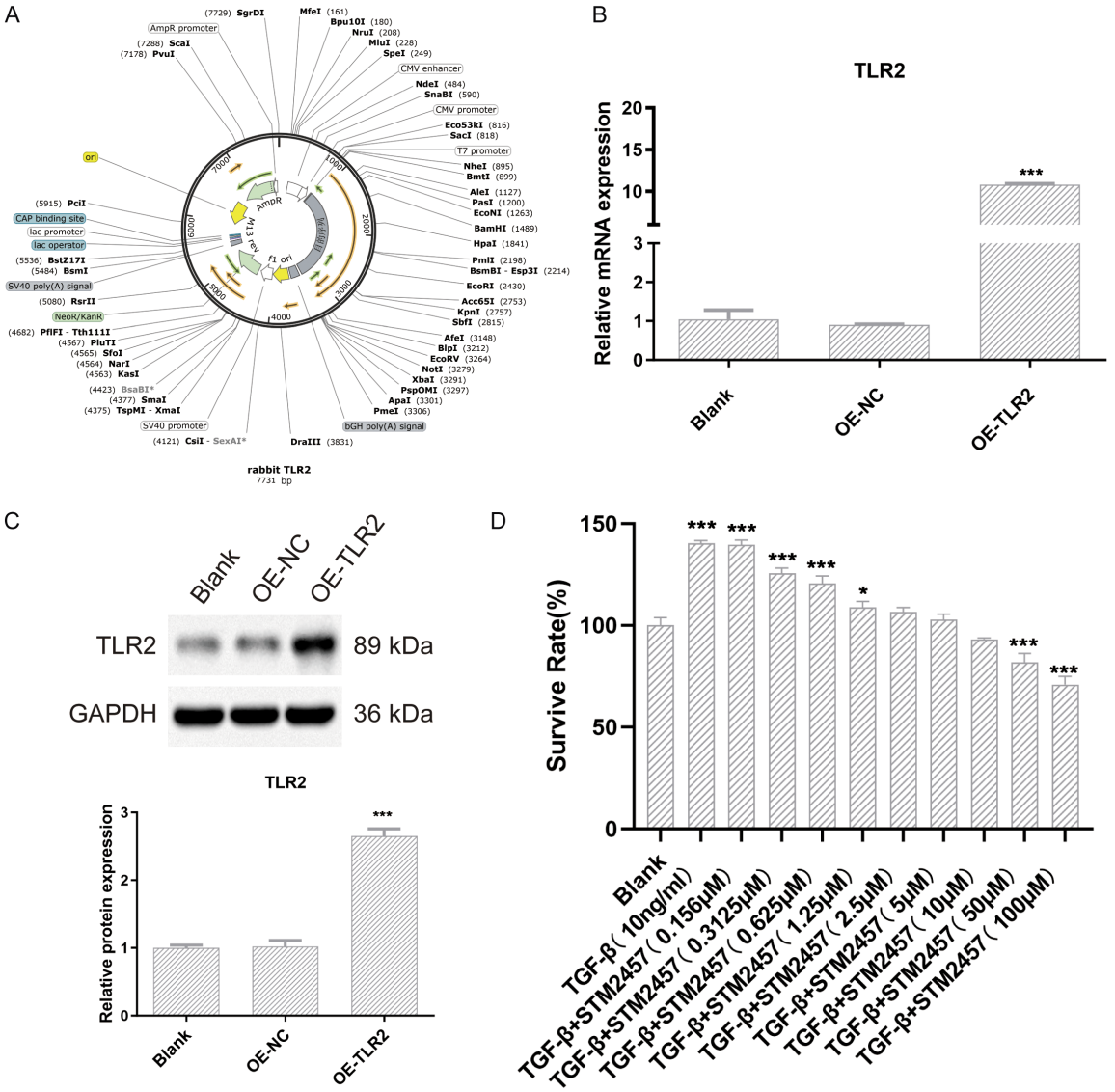

Figure 5. Construction and validation of the TLR2 overexpression vector and evaluation of STM2457 effects. (A) Plasmid map of the TLR2 overexpression vector; (B) qRT-PCR analysis of TLR2 mRNA expression follosing transfection with the TLR2 overexpression vector (n=6); (C) Western blot analysis of TLR2 protein expression following transfection with the TLR2 overexpression vector (n=3); (D) Validation of the inhibitory effect of the METTL3 methyltransferase inhibitor STM2457 (n=3). Note: Data are presented as mean ± SEM. Comparisons among groups were performed using one-way ANOVA with Dunnett's post hoc test. *P<0.05, ***P<0.001, ns: not significant.

tor, STM2457, was applied at an optimized concentration of 10 μM (**Figure 5D**).

Functionally, ADSC-Exos significantly inhibited fibroblast proliferation, whereas this inhibitory effect was markedly attenuated by TLR2 overexpression or METTL3 inhibition with STM2457 (**Figure 6A**, **6B**). qPCR and Western blot analyses demonstrated that ADSC-Exos downregulated the expression of α-SMA, type I collagen, TLR2, PI3K, and AKT, while TLR2 overexpression or STM2457 treatment partially reversed these effects (**Figure 6C**, **6D**). Moreover, the increase in global m6A levels induced by ADSC-Exos was significantly reduced by TLR2 overexpression and further diminished following STM2457 treatment (**Figure 6E**). Finally, wound healing assays confirmed that the inhibitory effect of ADSC-Exos on fibroblast migration was likewise reversed by TLR2 overexpression or METTL3 inhibition (**Figure 6F**, **6G**).

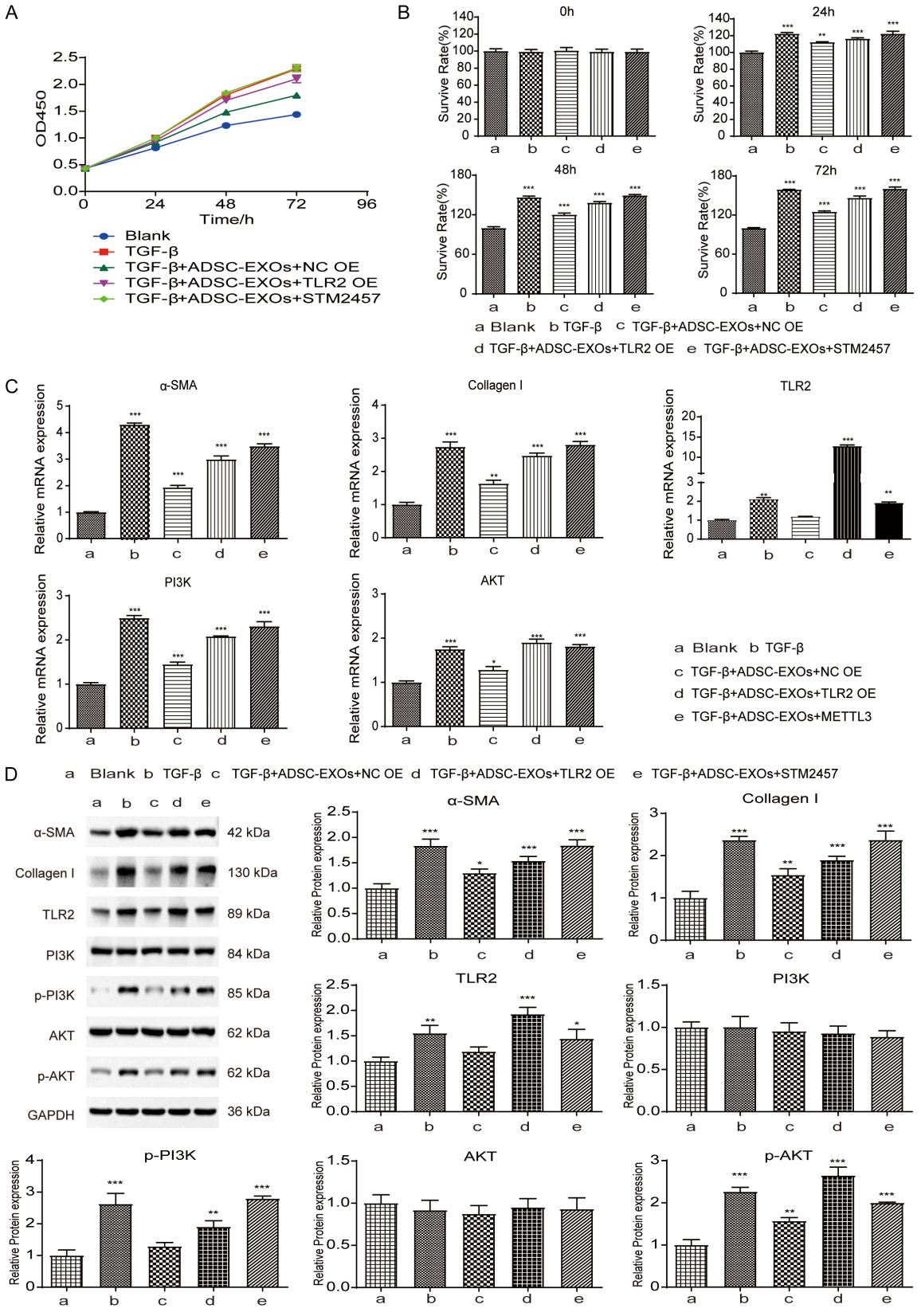
A
OD450
Time/h
Blank
TGF-β
TGF-β+ADSC-EXOs+NC OE
TGF-β+ADSC-EXOs+TLR2 OE
TGF-β+ADSC-EXOs+STM2457
B
0h
24h
48h
72h
Survive Rate(%)
a Blank b TGF-β c TGF-β+ADSC-EXOs+NC OE
d TGF-β+ADSC-EXOs+TLR2 OE e TGF-β+ADSC-EXOs+STM2457
C
α-SMA
Collagen I
TLR2
PI3K
AKT
Relative mRNA expression
a Blank b TGF-β
c TGF-β+ADSC-EXOs+NC OE
d TGF-β+ADSC-EXOs+TLR2 OE
e TGF-β+ADSC-EXOs+METTL3
D
a Blank b TGF-β c TGF-β+ADSC-EXOs+NC OE d TGF-β+ADSC-EXOs+TLR2 OE e TGF-β+ADSC-EXOs+STM2457
α-SMA 42 kDa
Collagen I 130 kDa
TLR2 89 kDa
PI3K 84 kDa
p-PI3K 85 kDa
AKT 62 kDa
p-AKT 62 kDa
GAPDH 36 kDa
Relative Protein expression
p-PI3K
p-AKT

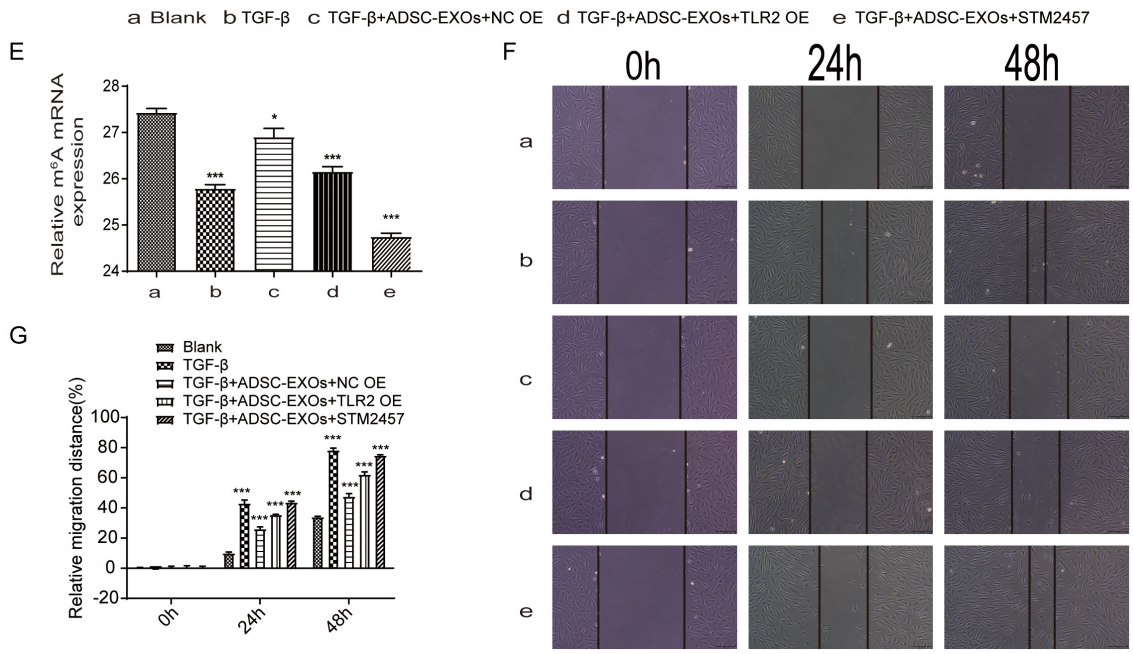

Figure 6. Effects of TLR2 and METTL3 modulation on fibroblast phenotypes following ADSC-Exos treatment. (A, B) Effects of TLR2 overexpression and METTL3 inhibition on fibroblast viability following ADSC-Exos treatment (n=6); (C) Effects of TLR2 overexpression and METTL3 inhibition on mRNA expression levels of α-SMA, collagen I, TLR2, PI3K and AKT following ADSC-Exos treatment (n=6); (D) Effects of TLR2 overexpression and METTL3 inhibition on protein expression levels of α-SMA, collagen I, TLR2, PI3K, and AKT following ADSC-Exos treatment (n=3); (E) Effects of TLR2 overexpression and METTL3 inhibition on global m6A levels following ADSC-Exos treatment (n=6); (F, G) Effects of TLR2 overexpression and METTL3 inhibition on fibroblast migration following ADSC-Exos treatment (n=6). Notes: Data are presented as mean ± SEM. For comparisons involving multiple groups and time points, two-way ANOVA with Sidak's post hoc test was used. *P<0.05, *P<0.01, ns: not significant.

Discussion

In recent years, interventional pulmonology has advanced rapidly, with endovascular interventions becoming the primary approach for managing benign airway stenosis. However, secondary injury during procedures often induces excessive granulation tissue formation and scar contracture, leading to restenosis rates as high as 10%-50% [34-38]. This study focuses on fibroblasts-to-myofibroblasts transdifferentiation and investigates the regulatory role of ADSC-derived exosomes (ADSC-Exos) in this process and the underlying mechanisms.

Local administration of ADSC-Exos effectively reduced the expression of α-SMA and type I collagen in airway tissues. Mechanistically, ADSC-Exos increased global m6A levels by upregulating the m6A methyltransferase METTL3, whereas METTL3 knockdown reversed the inhibitory effects of exosomes on myofibroblast differentiation. Through integrated analysis of MeRIP-seq and RNA-seq data, TLR2 was identified as a key downstream target. Following ADSC-Exos treatment, m6A methylation levels of TLR2 transcripts were markedly increased, while TLR2 mRNA expression was correspondingly decreased. Notably, TLR2 has been reported to be closely associated with the PI3K-AKT signaling pathway [39-42].

Functional experiments further confirmed that ADSC-Exos upregulate METTL3, thereby enhancing m6A methylation of TLR2 mRNA and promoting its downregulation. This, in turn, suppresses activation of the PI3K-AKT pathway and inhibits fibroblasts-to-myofibroblast transdifferentiation, as evidenced by reduced cell proliferation, migration, and expression of myofibroblast-associated markers. Thes effects were reversed by TLR2 overexpression or METTL3 inhibition. Collectively, these findings indicate that ADSC-Exos exert their antifibrotic effects through the METTL3/TLR2/PI3K-AKT regulatory axis.

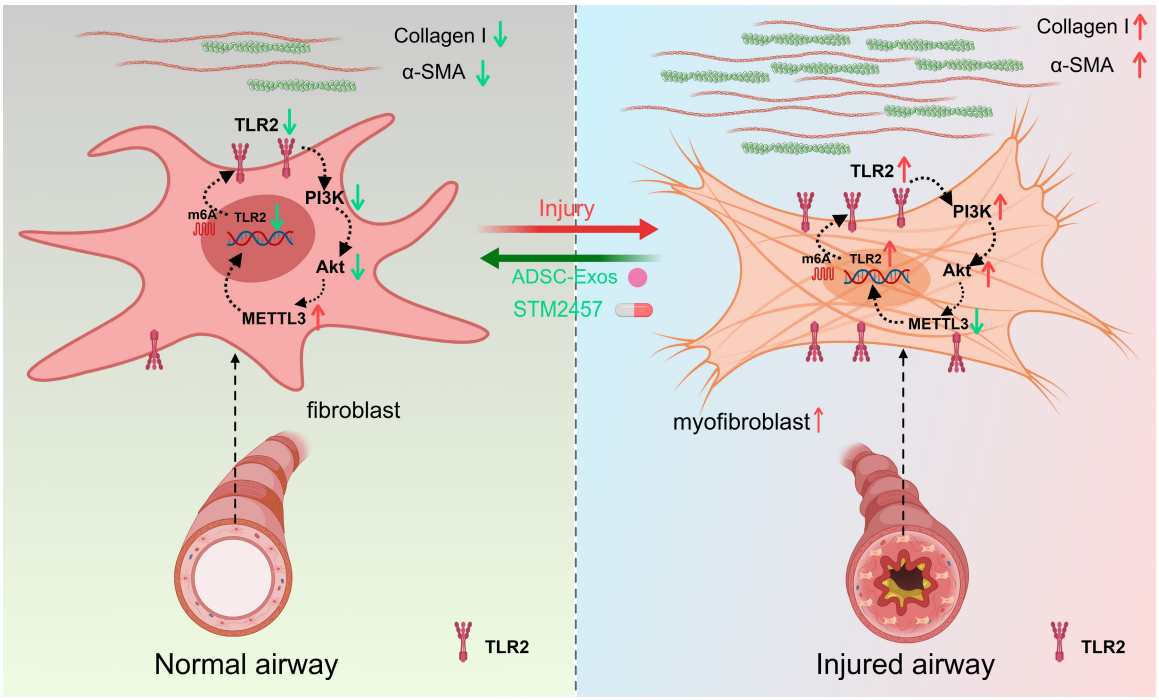

Figure 7. Schematic illustration of the mechanism by which ADSC-Exos inhibit myofibroblast transdifferentiation and promote airway repair. ADSC-Exos enhance METTL3-mediated m6A methylation of TLR2 mRNA, leading to reduced TLR2 expression and suppression of the TLR2/PI3K-AKT signaling pathway, thereby inhibiting fibroblast-to-myofibroblast transdifferentiation and promoting airway repair.

In this study, *in vivo* assessments were conducted one week after intervention, corresponding to the granulation phase of airway repair, based on previously established models [33]. Although the present work reveals a novel mechanism by which ADSC-Exos inhibit the PI3K-AKT pathway via METTL3-mediated m6A modification of TLR2, several limitations should be acknowledged. First, the findings are primarily based on a rabbit airway injury model. While informative, interspecies differences in airway anatomy, immune responses, nd repair mechanisms exist between rabbits and humans [43]. Moreover, the complexity of the *in vivo* microenvironment, including inflammatory infiltration and mechanical stress, cannot be fully recapitulated by the *in vitro* TGF-β-induced fibroblast model [44, 45]. Second, the observation period was limited to the early granulation phase. The long-term therapeutic efficacy, functional outcomes, and safety profile of ADSC-Exos treatment, including potential immunogenicity and tumorigenicity, remain to be determined. Third, challenges in exosome preparation and standardization persist. The yield, molecular cargo, and biological activity of ADSC-Exos may vary substantially depending on donor characteristics and isolation protocols [20, 22, 23]. Although MSC-derived exosomes are generally considered to have low immunogenicity [46, 47], batch-to-batch heterogeneity represents a major obstacle to clinical reproducibility and large-scale application. Fourth, this study primarily focused on the TLR2-PI3K axis. However, airway fibrosis is regulated by multiple signaling pathways, including TGF-β/Smad, Wnt/β-catenin signaling, as well as diverse cell populations [48-50]. Whether ADSC-Exos modulate these additional pathways warrants further investigation [16, 51]. Finally, the assessment of fibrosis was limited to α-SMA and collagen I expression. A more comprehensive evaluation, incorporating additional profibrotic markers (e.g., TGF-β1, CTGF, MMPs/TIMPs) and quantitative histopathological analyses, such as Masson's trichrome staining over extended time points, would provide a more complete understanding of the anti-fibrotic effects of ADSC-Exos.

Future studies should validate these mechanisms in more clinically relevant animal models

and examine the correlation between METTL3, TLR2, and m6A in modification during disease progression in human clinical samples [52]. In parallel, further investigation is required to determine whether METTL3-mediated m6A modification regulates additional fibrotic signaling pathways. From a translational perspective, the development of engineered ADSC-Exos with enhanced targeting or defined molecular cargo may facilitate combination strategies with existing antifibrotic drugs or interventional therapies. Moreover, long-term animal studies are needed to systematically evaluate sustained airway patency and assess potential safety risks.

Conclusion

From a novel epigenetic perspective, this study demonstrates for the first time that ADSC-Exos effectively block fibroblast to myofibroblast transdifferentiation. This effect is mediated by upregulation of METTL3, which increases m6A methylation of TLR2 mRNA, downregulates TLR2 expression, and ultimately suppresses activation of the PI3K-AKT pathway (**Figure 7**). Through this regulatory axis, ADSC-Exos promote airway repair and limit scar-associated narrowing. These findings provide mechanistic insight into the high recurrence rate of benign airway stenosis and establish a theoretical foundation for the development of standardized and scalable therapies based on ADSC-Exos or their key molecular effectors. Future research should focus on addressing current limitations, refining therapeutic strategies, and advancing toward clinical translation.

Acknowledgements

We sincerely thank Master Yaotang Fang, Master Kai Zhang, and Dr. Zhihui Fu for their expert technical support during this research. Their precise experimental work and scientific expertise were essential to this study. Special gratitude is extended to the staff of the Medical Research Center of Quanzhou Medical College for instrument support. This work was funded by Fujian Provincial Health Technology Project (No. 2021QNA069), the Quanzhou City Science & Technology Program of China (No. 2021N079S), the Natural Science Foundation of Fujian Province(2024J011519), and the Opening Project of Fujian Key Laboratory of Lung Stem Cells (No. FGXB202404).

Disclosure of conflict of interest

None.

Address correspondence to: Guoying Zhang, Department of Pulmonary and Critical Care Medicine, Quanzhou First Hospital Affiliated to Fujian Medical University, Anji South Road No. 1028, Fengze District, Quanzhou 362000, Fujian, China. E-mail: zhangguoying@fjmu.edu.cn

References

[1] Oberg CL, Holden VK and Channick CL. Benign central airway obstruction. Semin Respir Crit Care Med 2018; 39: 731-746.

[2] Murgu SD, Egressy K, Laxmanan B, Doblare G, Ortiz-Comino R and Hogarth DK. Central airway obstruction: benign strictures, tracheobronchomalacia, and malignancy-related obstruction. Chest 2016; 150: 426-441.

[3] Barros Casas D, Fernández-Bussy S, Folch E, Flandes Aldeyturriaga J and Majid A. Non-malignant central airway obstruction. Arch Bronconeumol 2014; 50: 345-354.

[4] Zhang M, Han W, Tang H, Li G, Zhang M, Xu R, Liu Y, Yang T, Li W, Zou J and Wu K. Genomic diversity dynamics in conserved chicken populations are revealed by genome-wide SNPs. BMC Genomics 2018; 19: 598.

[5] Shaw TJ and Martin P. Wound repair: a showcase for cell plasticity and migration. Curr Opin Cell Biol 2016; 42: 29-37.

[6] Amini-Nik S, Cambridge E, Yu W, Guo A, Whetstone H, Nadesan P, Poon R, Hinz B and Alman BA. β-Catenin-regulated myeloid cell adhesion and migration determine wound healing. J Clin Invest 2014; 124: 2599-2610.

[7] Zhang Y, Wang J, Li H, Yuan L, Wang L, Wu B and Ge J. Hydrogen sulfide suppresses transforming growth factor-β1-induced differentiation of human cardiac fibroblasts into myofibroblasts. Sci China Life Sci 2015; 58: 1126-1134.

[8] Walker EJ, Heydet D, Veldre T and Ghildyal R. Transcriptomic changes during TGF-β-mediated differentiation of airway fibroblasts to myofibroblasts. Sci Rep 2019; 9: 20377.

[9] D'Urso M and Kurniawan NA. Mechanical and physical regulation of fibroblast-myofibroblast transition: from cellular mechanoresponse to tissue pathology. Front Bioeng Biotechnol 2020; 8: 609653.

[10] Nürnberger S, Lindner C, Maier J, Strohmeier K, Wurzer C, Slezak P, Suessner S, Holnthoner W, Redl H, Wolbank S and Priglinger E. Adipose-tissue-derived therapeutic cells in their natural environment as an autologous cell therapy strategy: the microtissue-stromal vas-

cular fraction. Eur Cell Mater 2019; 37: 113-133.
[11] Strong AL, Neumeister MW and Levi B. Stem cells and tissue engineering: regeneration of the skin and its contents. Clin Plast Surg 2017; 44: 635-650.
[12] Taverna S, Pucci M and Alessandro R. Extracellular vesicles: small bricks for tissue repair/regeneration. Ann Transl Med 2017; 5: 83.
[13] Ghosh D, McGrail DJ and Dawson MR. TGF-β1 pretreatment improves the function of mesenchymal stem cells in the wound bed. Front Cell Dev Biol 2017; 5: 28.
[14] Gong M, Yu B, Wang J, Wang Y, Liu M, Paul C, Millard RW, Xiao DS, Ashraf M and Xu M. Mesenchymal stem cells release exosomes that transfer miRNAs to endothelial cells and promote angiogenesis. Oncotarget 2017; 8: 45200-45212.
[15] Zhang B, Wu X, Zhang X, Sun Y, Yan Y, Shi H, Zhu Y, Wu L, Pan Z, Zhu W, Qian H and Xu W. Human umbilical cord mesenchymal stem cell exosomes enhance angiogenesis through the Wnt4/β-catenin pathway. Stem Cells Transl Med 2015; 4: 513-522.
[16] Wang X, Gu H, Qin D, Yang L, Huang W, Essandoh K, Wang Y, Caldwell CC, Peng T, Zingarelli B and Fan GC. Exosomal miR-223 contributes to mesenchymal stem cell-elicited cardioprotection in polymicrobial sepsis. Sci Rep 2015; 5: 13721.
[17] Bi Z, Liu Y, Zhao Y, Yao Y, Wu R, Liu Q, Wang Y and Wang X. A dynamic reversible RNA N6 -methyladenosine modification: current status and perspectives. J Cell Physiol 2019; 234: 7948-7956.
[18] Tsai YC, Hsieh TH, Liao YR, Tsai MT, Lin TP, Lee DY, Park J, Kim D, Susztak K, Yang SF, Lin CC and Li SY. METTL3-mediated N 6 -methyladenosine mRNA modification and cGAS-STING pathway activity in kidney fibrosis. J Am Soc Nephrol 2024; 35: 1312-1329.
[19] Wang M, Hao Y, He W, Jia H, Zhong Z and Xia S. Nebulized mesenchymal stem cell-derived exosomes attenuate airway inflammation in a rat model of chronic obstructive pulmonary disease. Cell Immunol 2025; 409-410: 104933.
[20] Shen T, Zheng QQ, Shen J, Li QS, Song XH, Luo HB, Hong CY and Yao K. Effects of adipose-derived mesenchymal stem cell exosomes on corneal stromal fibroblast viability and extracellular matrix synthesis. Chin Med J (Engl) 2018; 131: 704-712.
[21] Delmonte OM and Fleisher TA. Flow cytometry: surface markers and beyond. J Allergy Clin Immunol 2019; 143: 528-537.
[22] Wu B, Feng J, Guo J, Wang J, Xiu G, Xu J, Ning K, Ling B, Fu Q and Xu J. ADSCs-derived exosomes ameliorate hepatic fibrosis by suppressing stellate cell activation and remodeling hepatocellular glutamine synthetase-mediated glutamine and ammonia homeostasis. Stem Cell Res Ther 2022; 13: 494.
[23] Shen T, Shen J, Zheng QQ, Li QS, Zhao HL, Cui L and Hong CY. Cell viability and extracellular matrix synthesis in a co-culture system of corneal stromal cells and adipose-derived mesenchymal stem cells. Int J Ophthalmol 2017; 10: 670-678.
[24] Wang M, Hao Y, He W, Jia H, Zhong Z and Xia S. Nebulized mesenchymal stem cell-derived exosomes attenuate airway inflammation in a rat model of chronic obstructive pulmonary disease. Cell Immunol 2025; 409-410: 104933.
[25] Zhao B, Zhang Y, Han S, Zhang W, Zhou Q, Guan H, Liu J, Shi J, Su L and Hu D. Exosomes derived from human amniotic epithelial cells accelerate wound healing and inhibit scar formation. J Mol Histol 2017; 48: 121-132.
[26] Georgakopoulou VE, Lempesis IG, Sklapani P, Trakas N and Spandidos DA. Exploring the pathogenetic mechanisms of Mycoplasmapneumoniae (review). Exp Ther Med 2024; 28: 271.
[27] Yankova E, Blackaby W, Albertella M, Rak J, De Braekeleer E, Tsagkogeorga G, Pilka ES, Aspris D, Leggate D, Hendrick AG, Webster NA, Andrews B, Fosbeary R, Guest P, Irigoyen N, Eleftheriou M, Gozdecka M, Dias JML, Bannister AJ, Vick B, Jeremias I, Vassiliou GS, Rausch O, Tzelepis K and Kouzarides T. Small-molecule inhibition of METTL3 as a strategy against myeloid leukaemia. Nature 2021; 593: 597-601.
[28] Seervi M, Sobhan PK, Joseph J, Mathew KA and Santhoshkumar TR. Correction to: ERO1α-dependent endoplasmic reticulum-mitochondrial calcium flux contributes to ER stress and mitochondrial permeabilization by procaspase-activating compound-1 (PAC-1). Cell Death Dis 2025; 16: 740.
[29] Xu QC, Tien YC, Shi YH, Chen S, Zhu YQ, Huang XT, Huang CS, Zhao W and Yin XY. METTL3 promotes intrahepatic cholangiocarcinoma progression by regulating IFIT2 expression in an m6A-YTHDF2-dependent manner. Oncogene 2022; 41: 1622-1633.
[30] Ming Q, Li Z, Tan J and Li Y. Adenosine A1 receptor agonist alleviates cerebral ischemia/reperfusion injury by inhibiting Nrf2/NLRP3 signaling-mediated pyroptosis. Exp Ther Med 2025; 29: 94.
[31] Luo G, Zhu T and Ren Z. METTL3 Regulated the meat quality of Rex rabbits by controlling PCK2 expression via a YTHDF2-N6-methyladenosine axis. Foods 2022; 11: 1549.

[32] Lei Y, Deng X, Zhang Z and Chen J. Natural product procyanidin B1 as an antitumor drug for effective therapy of colon cancer. Exp Ther Med 2023; 26: 506.
[33] Zhang G, Wang J and Zeng Y. A modified rabbit model of tracheal stenosis and a household endoscope. More simplicity and accessibility. Acta Cir Bras 2020; 35: e351104.
[34] Dalar L, Karasulu L, Abul Y, Özdemir C, Sökücü SN, Tarhan M and Altin S. Bronchoscopic treatment in the management of benign tracheal stenosis: choices for simple and complex tracheal stenosis. Ann Thorac Surg 2016; 101: 1310-1317.
[35] Guibert N, Saka H and Dutau H. Airway stenting: technological advancements and its role in interventional pulmonology. Respirology 2020; 25: 953-962.
[36] Emam W, Mostafa Y, Madkour A, Wagih K, Ezzelregal H, Anagnostopoulos N and Stratakos G. Bronchoscopic management as an alternative treatment in non-operable benign tracheal stenosis. Int J Clin Pract 2021; 75: e14058.
[37] Freitag L and Darwiche K. Endoscopic treatment of tracheal stenosis. Thorac Surg Clin 2014; 24: 27-40.
[38] Jeong BH, Ng J, Jeong SH and Kim H. Clinical outcomes of complications following self-expandable metallic stent insertion for benign tracheobronchial stenosis. Medicina (Kaunas) 2020; 56: 367.
[39] Guo XL, Gao YY, Yang YX, Zhu QF, Guan HY, He X, Zhang CL, Wang Y, Xu GB, Zou SH, Wei MC, Zhang J, Zhang JJ and Liao SG. Amelioration effects of α-viniferin on hyperuricemia and hyperuricemia-induced kidney injury in mice. Phytomedicine 2023; 116: 154868.
[40] Kim SM, Park S, Hwang SH, Lee EY, Kim JH, Lee GS, Lee G, Chang DH, Lee JG, Hwang J, Lee Y, Kyung M, Kim EK, Kim JH, Kim TH, Moon JH, Kim BC, Ko G, Kim SY, Ryu JH, Lee JS, Lee CH, Kim JY, Kim S, Lee WJ and Kim MH. Secreted Akkermansia muciniphila threonyl-tRNA synthetase functions to monitor and modulate immune homeostasis. Cell Host Microbe 2023; 31: 1021-1037, e10.
[41] Zhang W, Liu W and Hu X. Robinin inhibits pancreatic cancer cell proliferation, EMT and inflammation via regulating TLR2-PI3k-AKT signaling pathway. Cancer Cell Int 2023; 23: 328.
[42] Yu G, Yu H, Yang Q, Wang J, Fan H, Liu G, Wang L, Bello BK, Zhao P, Zhang H and Dong J. Vibrio harveyi infections induce production of proinflammatory cytokines in murine peritoneal macrophages via activation of p38 MAPK and NF-κB pathways, but reversed by PI3K/AKT pathways. Dev Comp Immunol 2022; 127: 104292.
[43] Steehler MK, Hesham HN, Wycherly BJ, Burke KM and Malekzadeh S. Induction of tracheal stenosis in a rabbit model-endoscopic versus open technique. Laryngoscope 2011; 121: 509-514.
[44] Tomcik M, Palumbo-Zerr K, Zerr P, Avouac J, Dees C, Sumova B, Distler A, Beyer C, Cerezo LA, Becvar R, Distler O, Grigorian M, Schett G, Senolt L and Distler JH. S100A4 amplifies TGF-β-induced fibroblast activation in systemic sclerosis. Ann Rheum Dis 2015; 74: 1748-1755.
[45] Son M, Kim GY, Yang Y, Ha S, Kim J, Kim D, Chung HY, Moon HR and Chung KW. PPAR pan agonist MHY2013 alleviates renal fibrosis in a mouse model by reducing fibroblast activation and epithelial inflammation. Int J Mol Sci 2023; 24: 4882.
[46] Tang A, Shu Q, Jia S, Lai Z and Tian J. Adipose mesenchymal stem cell-derived exosomes as nanocarriers for treating musculoskeletal disorders. IJN 2024; 19:13547-13562.
[47] Zhang X, Jiang Y, Huang Q, Wu Z, Pu H, Xu Z, Li B, Lu X, Yang X, Qin J and Peng Z. Exosomes derived from adipose-derived stem cells overexpressing glyoxalase-1 protect endothelial cells and enhance angiogenesis in type 2 diabetic mice with limb ischemia. Stem Cell Res Ther 2021; 12: 403.
[48] Friedman RM, Truong HD, Aronson MR, Brown EA, Angelozzi M, Chen JF, Zur KB, Lefebvre V and Gottardi R. Inhibition of the MRTF-A/SRF signaling axis alleviates vocal fold scarring. Matrix Biol 2025; 137: 1-11.
[49] Schilter H, Cantemir-Stone CZ, Leksa V, Ohradanova-Repic A, Findlay AD, Deodhar M, Stockinger H, Song X, Molloy M, Marsh CB and Jarolimek W. The mannose-6-phosphate analogue, PXS64, inhibits fibrosis via TGF-β1 pathway in human lung fibroblasts. Immunol Lett 2015; 165: 90-101.
[50] He L, Zhu C, Jia J, Hao XY, Yu XY, Liu XY and Shu MG. ADSC-Exos containing MALAT1 promotes wound healing by targeting miR-124 through activating Wnt/β-catenin pathway. Biosci Rep 2020; 40: BSR20192549.
[51] Ren H, Su P, Zhao F, Zhang Q, Huang X, He C, Wu Q, Wang Z, Ma J and Wang Z. Adipose mesenchymal stem cell-derived exosomes promote skin wound healing in diabetic mice by regulating epidermal autophagy. Burns Trauma 2024; 12: tkae001.
[52] Schwartz GS, Razi SS, Belsley SJ, Boone D, Latif MJ, Connery CP, Lebovics RS and Bhora FY. Endoscopic tracheoplasty: segmental tracheal ring resection in a porcine model. J Bronchology Interv Pulmonol 2010; 17: 232-235.

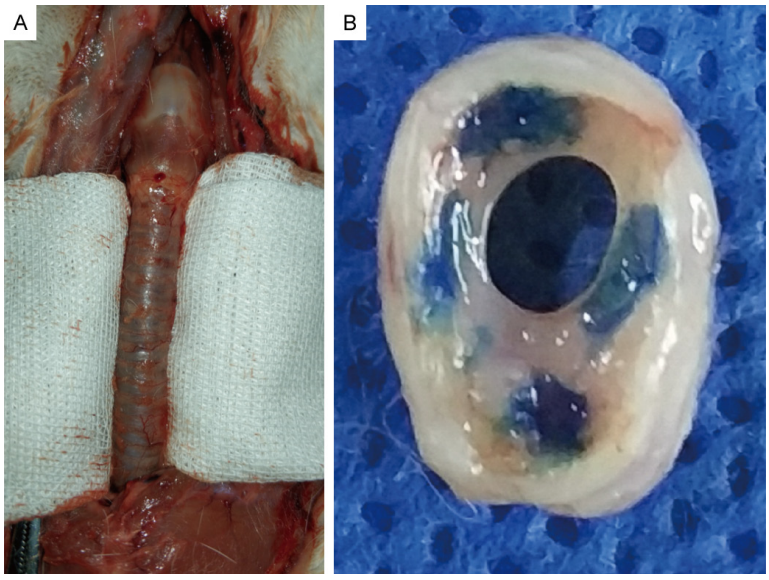

Figure S1. Macroscopic examination after drug injection at the site of tracheal stenosis. A. No obvious abnormal damage was observed on the anterior wall of the trachea and the anterior cervical region; B. The cross-section of the trachea at the injection site showed that methylene blue could be injected into the local tissue of the tracheal wall as expected.

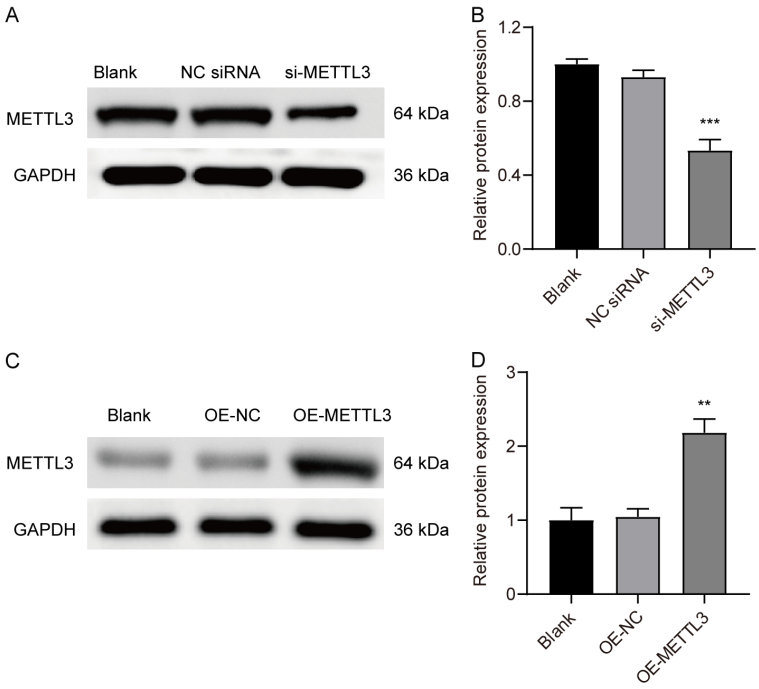

Figure S2. Western Blot analysis of METTL3 siRNA/overexpression vectors transfection efficiency in transfected cells. A, B. Results of METTL3 protein silencing by siRNA, each bar represents the mean ± SEM (n=3); C, D. Results of METTL3 protein overexpression by overexpression vectors, each bar represents the mean ± SEM (n=3). **P<0.01; ***P<0.001. TLR2 overexpression vector: OE-TLR2 (TLR2 overexpression vector) Group, the TLR2 protein expression was increased (**Figure 5B**), TLR2 mRNA expression was increased (**Figure 5C**).

nanofcm

Comprehensive Bio-Nanoparticle Analysis
Nano-Flow Cytometry

Size & Concentration Report

2 9×

Data File	20231227 2 9× 5.nfa	Population	Total

SN: FNAN30E20071514
Software: V2.0
Sample Pressure: 1.0Kpa

Laser: 5/40 mW 488
SS Decay: 10%
Threshold/sub: 75.1 9.1 1.2 1/0 0 0 0
Min Width: 0.3 ms

Total Size Infomation

Gating Range 30 - 150 nm

All Events	2952	
Gating Events	2811	
% of all	95.22	
Median	79.2	nm
Mean	84.4	nm
Std Dev.	18.0	nm

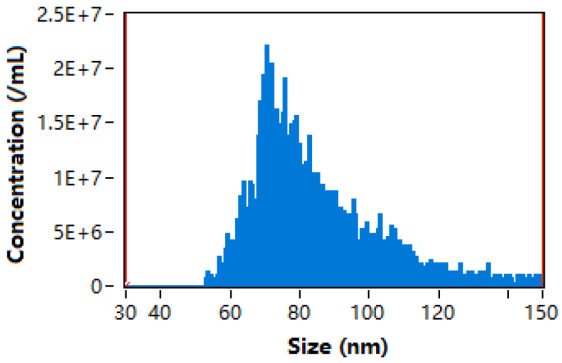

Total Concentration Infomation

	Particle Number	Dilution Factor
STD	5765	100
Blank	45	———
Sample	2997	9

STD Con.	2.22E+10	Particles/mL
Sample Flow Rate	25.97	nL/min
Sample Con.	1.02E+9	Particles/mL

Corrected Ratio: 2952/2952 100.0%

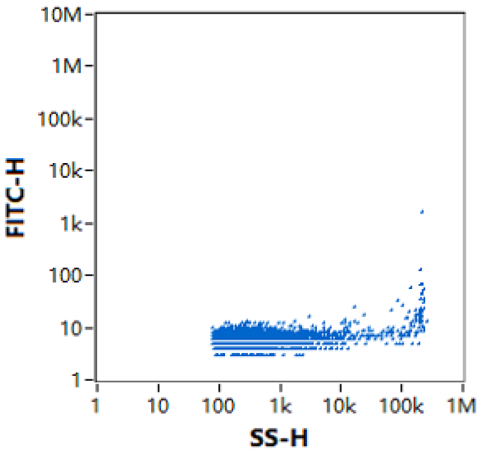

Report By :

2023/12/27 10:30

Figure S3. Exosome particle concentration.

Table S1. The sequence of siRNAs

NC siRNA	sense 5'-UUCUCCGAACGUGUCACGUTT-3'
	antisense 5'-ACGUGACACGUUCGGAGAATT-3'
METTL3 siRNA	sense 5'-CUAAGGAACAACAGAGCAATT-3'
	antisense 5'-UUGCUCUGUUGUUCCUUAGTT-3'

Table S2. Exosome mass concentration by BCA

Project Number	231021773
Sample Number	A32
Absorbance Value A1	0.115
Absorbance Value A2	0.115
Average Absorbance Value A	0.115
Concentration after Sample Lysis (μg/μL)	0.008434
Original Sample Concentration (μg/μL)	0.04217
Note: Diluted 4 times for detection	
Exosome Volume μL	100
μg/μL	4.217